Co-Ion Desorption as the Main Charging Mechanism in Metallic 1T-MoS_2 Supercapacitors

Sheng Bi[1,2] and Mathieu Salanne[1,2,3,*]

[1]*Sorbonne Université, CNRS, Physico-Chimie des Électrolytes et Nanosystèmes Interfaciaux, PHENIX, F-75005 Paris, France*

[2]*Réseau sur le Stockage Électrochimique de l'Énergie (RS2E), FR CNRS 3459, 80039 Amiens Cedex, France*

[3]*Institut Universitaire de France (IUF), 75231 Paris Cedex 05, France*

E-mail : mathieu.salanne@sorbonne-universite.fr

Abstract

Metallic 1T-MoS_2 is a promising electrode material for supercapacitors applications. Its layered structure allows the efficient intercalation of ions, leading to experimental volumetric capacitance as high as 140 F/cm^3. Molecular dynamics could in principle be used to characterize its charging mechanism, however, unlike conventional nanoporous carbon, 1T-MoS_2 is a multi-component electrode. The Mo and S atoms have very different electronegativities, so that 1T-MoS_2 cannot be simulated accurately using the conventional constant potential method. In this work, we show that controlling the electrochemical potential of the atoms allows to recover average partial charges for the elements in agreement with electronic structure calculations for the material at rest, without compromising the ability to simulate systems under an applied voltage. The simulations yield volumetric capacitances in agreement with experiments. We show that due to the large electronegativity of S, the co-ion desorption is the main charging mechanism at play during the charging process. This contrast drastically with carbon materials for which ion exchange and counter-ion adsorption usually dominate. In the future, our method can be extended to the study of a wide range family of 2D layered materials such as MXenes.

Keywords: Metallic transition metal dichalcogenides, Supercapacitors, Charging mechanism, Nanopores

Introduction

Two-dimensional transition metal dichalcogenides are an emerging class of layered materials with versatile physical and chemical properties.[1,2] Among them, 2D molybdenum disulfide (MoS_2) has attracted considerable attention because of its potential and promising application in a variety of fields,[3–5] such as nanoelectronics,[6,7] nanophotonics,[8,9] sensor,[10,11] catalysis,[12,13] water desalination,[14,15] etc. In particular, although the crystalline 2H-MoS_2 phase is semi-conducting,[16] it can be exfoliated to form a conductive 1T-MoS_2 phase[17] that can be used as an electrode for energy storage applications.[18–20]

Supercapacitors are electrochemical energy devices in which electrons are stored through the adsorption of ions on metallic electrodes upon application of a voltage. Nanoporous materials are particularly attractive since they can accommodate large amounts of ions in a limited volume, thus increasing the energy density of the devices.[21] Exfoliated 2D materials, such as graphene and MXenes, have thus been extensively studied in recent years for this application.[22,23] Due to its excellent metallic properties, 1T-MoS_2 is one of the best candidates, and its capacitive properties were demonstrated by Acerce et al. both in aqueous and organic electrolytes.[17]

Over the past decade, molecular dynamics simulations have been used extensively to study the microscopic mechanisms at play in supercapacitors.[24–26] Good predictions of the capacitive,[24] as well as of the dynamic properties[47] of nanoporous carbon electrodes were allowed by the use of the so-called constant-potential method (CPM). In this method, the charges located on electrode atoms are allowed to fluctuate in order to keep the electrode potential (or rather the potential difference between the two capacitive electrodes) at a fixed value.[21] More recently, it was used to study a large range of supercapacitors electrode materials, ranging from zeolite-templated carbons[30] to metal-organic frameworks (MOFs)[26] and MoS_2.[46] However, a limitation of the CPM in the case of multi-component materials is the use of similar parameters for all the atom types, which thus respond in the same way to electrolyte fluctuations. Although this simplification may not have a large impact in the case of conductive MOFs, for which most of the chemical elements (C, N and O) will display similar partial charges, in the case of MoS_2 electronic structure

calculations yield very different charges for the two elements, which is attributed to their respective electronegativities.[37]

In this work we build on the extension of CPM by Onofrio and Strachan,[31] who proposed to control the electrochemical potential of the elements instead of the potential, leading to the CPM_χ method. We show that the simulated capacitance of 1T-MoS_2 nanosheets agrees with previous experimental work[17] using 1-ethyl-3-methylimidazolium tetrafluoroborate ([Emim][BF_4]) as the electrolyte ions. The simulations show that the charging mechanism is dominated by strong co-ion desorption effects, in contrast with previous simulations on 1T-MoS_2 using the CPM method and with other systems such as nanoporous carbons or MOFs. By studying the energetics of single ions adsorption, we show that this mechanism arises from the large electronegativity of surface sulfur atoms that drastically decreases the affinity of BF_4 anions. However, this effect only emerges under nanoconfinement conditions and not in the case of simple planar MoS_2 electrodes.

Results and Discussion

Capacitive performances of 1T-MoS_2 nanosheets

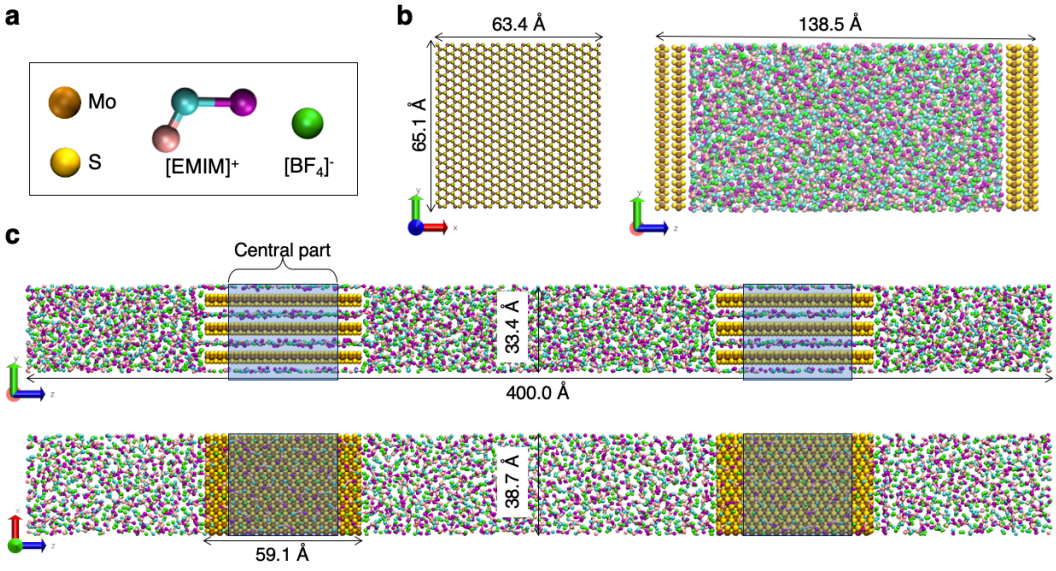

Fig. 1. MD simulations setup. a, Graphical representations of Mo and S atoms, and coarse-grained model of [EMIM][BF_4]. **b**, **c**, Snapshots of the simulated system with slab-shape MoS_2 electrodes (**b**) and with

1T-MoS_2 nanosheet electrodes (**c**). In the former, the blue regions represent the central part of the nanosheets, on which structural analyzes are performed.

The various simulated systems are displayed on **Fig. 1**. For each of them, MD simulations were performed at applied potentials of 0 V, 1 V, 2 V and 4 V using both CPM_χ and CPM for comparison purposes as discussed in the Methods section. We first focus on the capacitive properties of 1T-MoS_2 nanosheets, for which the spacing between the sheets was set accordingly to the experimental study of Acerce *et al.*[17]

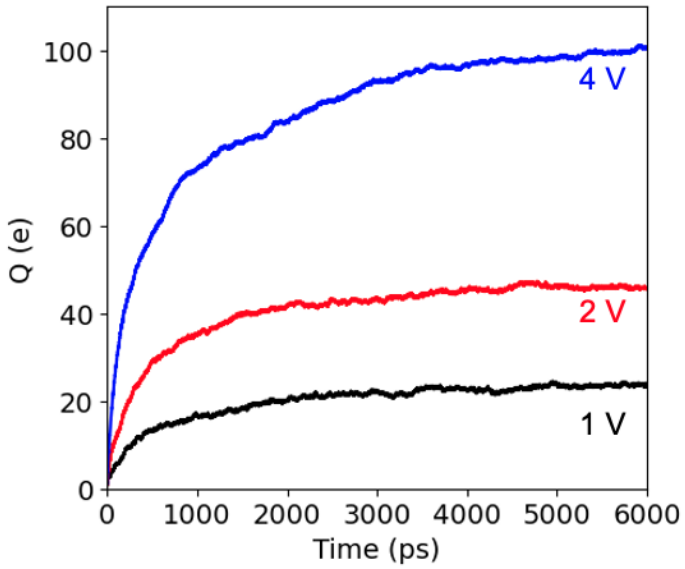

Fig. 2. Charging of 1T-MoS_2 nanosheets. Time evolutions of the total electrode charge, after voltages of 1 V, 2 V and 4 V were applied between two electrodes. The resulting specific capacitance (40.8 F/g at 4 V) is in good agreement with experiments (49.4 F/g).[17]

Fig. 2 shows the total charge on the positive electrode for applied potentials of 2 V and 4 V. The charging dynamics has a similar shape as in previous studies on nanoporous materials. From the equilibrium value, we can extract a specific capacitance of 40.8 F/g for each electrode at the largest applied potential of 4 V. This number is in good agreement with the experimental result, which is 49.4 F/g at the lowest scan rate measured.[17] The obtained difference (20%) is similar to what we observed in previous works on nanoporous carbons.[32] It is worth noting that in experiments, the [Emim][BF_4] was dissolved in acetonitrile

while in our case the neat ionic liquid is used. However, Acerce *et al.* reported that the adsorbed ions were desolvated, so that this should not affect much the final capacitance.[17]

Comparing the capacitances with other materials simulated under similar conditions, we observe that the specific capacitances are smaller than the ones typically obtained in nanoporous carbons (60 to 100 F/g in nanoporous graphene, 130 F/g in carbide-derived carbons[33]) or in MOFs (40 to 130 F/g).[34] However, the comparison is not very fair since the density of MoS_2, even exfoliated, is much larger than the one of these systems due to the presence of heavy Mo atoms. For practical applications, of equal importance is the volumetric capacitance. In contrast with Acerce *et al.*, who used the restacked material density to extract this quantity, we use the one obtained taking into account the larger spacing in the presence of adsorbed ions. This yields a volumetric capacitance of 113 F/cm^3 at 4 V. This number is as high as the one obtained in carbide-derived carbons (112 F/cm^3),[33] and larger than the one obtained in MOFs (which is below 110 F/cm^3)[34] confirming 1T-MoS_2, and more generally of layered sulfides,[35,36] as very strong candidates in future supercapacitor applications.

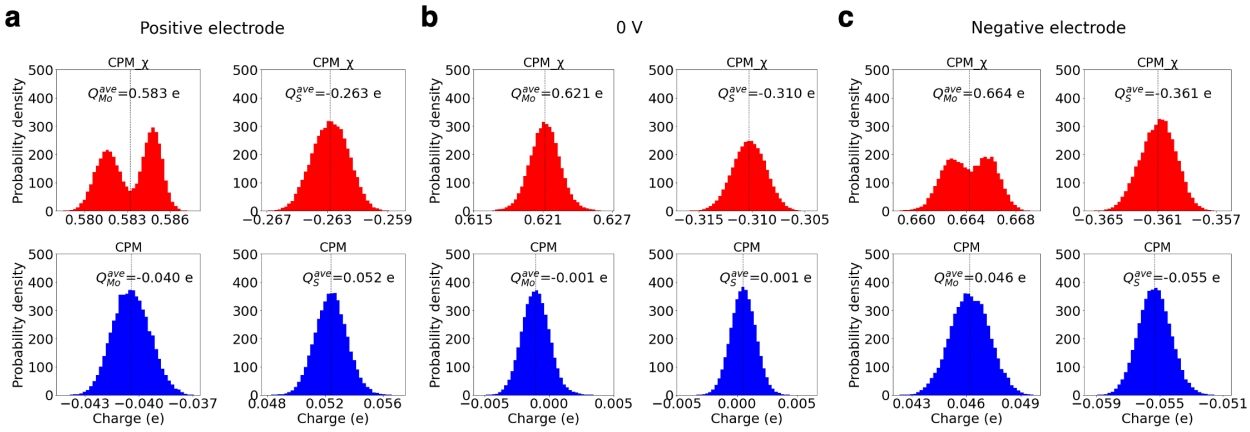

Fig. 3. Individual charges of the Mo and S atoms on electrified electrode. a, **b**, **c**, Histograms of charge per Mo and S atom on the positive electrode (**a**), on the electrode under 0 V (**b**), and on the negative electrode (**c**). For the polarized cases, the electric potential between the two electrodes is set to 2 V.

However, we note that the CPM simulations reported by Liang *et al.* reported a very similar specific capacitance (42 F/g).[46] It is therefore useful to compare the individual charges of the Mo and S atoms to

examine the reliability of the approaches. Two different scenarios can be observed in the CPM_χ and CPM cases (**Fig. 3**). When the electric potential is at 0 V (**Fig. 3b**), the average charge per Mo and per S atom in the CPM_χ case are +0.62 *e* and -0.31 *e*, respectively, which are very close to the DFT-obtained partial charge values (see Table 1 in the methods section);[37] whereas in the CPM case, the charges are both around zero. When the electrode is under positive polarization (**Fig. 3a**), in the original CPM simulation, the charge per S atom increases from zero to +0.052 *e* meanwhile the charge per Mo atom decreases from zero to -0.04 *e* during the charging; however, in the CPM_χ simulation, the charge per S atom rises from -0.31 *e* to -0.263 *e* whilst the charge per Mo atom decreases from +0.62 *e* to +0.583 e. This shows that despite a positive total charge on the electrode, the charge on the S atom of the positive electrode remains negative. Similarly, for the negative electrode (**Fig. 3c**), both methods give negative charges on S atoms and positive charges on Mo atoms but with quite different magnitudes: the final charge per S atom and per Mo atom in the CPM_χ simulation are -0.361 *e* and +0.664 e, respectively, whereas in the CPM simulation, these two values are -0.055 *e* and +0.046 *e* for S and Mo atoms, respectively.

The importance of representing accurately the electronic structure of MoS_2 surface was illustrated in the recent work of Tocci *et al.*, in which they compared its friction properties to the ones of graphene and hexagonal boron nitride using density functional theory-based molecular dynamics. From their calculations, they showed that the friction coefficient of water molecules on the three materials differ a lot, an effect which was attributed to the changing electrostatic interactions with the liquids.[38]

Impact of electronegativity effects on the adsorption mechanisms

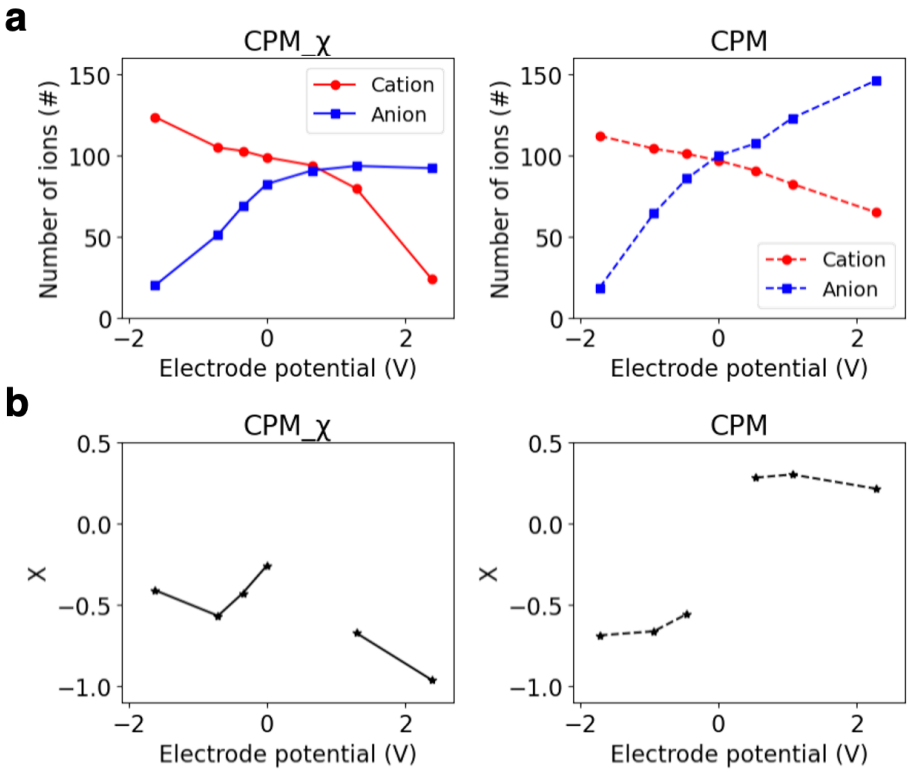

Fig. 4. Variation of in-pore ion population as a function of electrode potential. a, The number of ions inside the nanosheets for the CPM_χ simulations (left) and the CPM simulations (right). **b**, Charging mechanism parameter (X) obtained by the two methods. In both cases the electrode potential is defined as the potential between the electrode and the bulk-region electrolyte relative to its value at zero charge of the electrode.

It is therefore worthy studying the storage mechanism in the case where the simulations involve realistic atomic charges on the electrode atoms. To do so, we further analyze the ion populations inside the nanosheets as a function of electrode potential (**Fig. 4a**). Note that here the electrode potential is defined as the potential between the electrode and the bulk-region electrolyte relative to its value at zero charge of the electrode. One could see that despite resulting in similar capacitances, the CPM and CPM_χ methods give very different results for the in-pore cations and anions populations depending on the electrode polarization.

In particular, the number of adsorbed ions remains limited when using the CPM_χ, which shows that the high negative charge density on the S atoms confers them an ionophobic character.

In nanoporous supercapacitors, three different mechanisms are usually considered: counter-ion adsorption, co-ion desorption and ion exchange. Yet there is generally not a clear separation between the three, so that Forse *et al.* have introduced a charging parameter,[39] defined as:

$$X = \frac{N - N_0}{(N^{counter} - N^{co}) - (N_0^{counter} - N_0^{co})}$$

where N and N_0 are the total numbers of ions inside the electrode, respectively, at a working voltage and zero electrode potential ($N_{counter}$ and $N_0^{counter}$ for counterions and N_{co} and N_0^{co} for co-ions). Note that the charging mechanism parameter would be +1 (or −1) for pure permselective counterion adsorption (or co-ion desorption) and 0 for an exact one-to-one cation−anion exchange.

In the systems studied so far using MD or experimental techniques such as NMR,[39,40] the reported X values ranged between -0.36 and 0.7, indicating that ion exchange and counter-ion adsorption were the main charging mechanisms.[39,41] Similarly, electrochemical quartz crystal microbalance experiments show that these two mechanisms are at play in carbon materials with varying electrolytes.[42] As shown on **Fig. 4b**, here we observe a very different scenario for the 1T-MoS_2 nanoporous material. Firstly, in the case of the negative electrode, the two simulation methods point towards a charging mechanism mixing ion exchange and co-ion desorption. The co-ion desorption is more pronounced for the CPM (X=-0.6 to -0.7) than for the CPM_χ (which displays a non-monotonic variation of X between -0.3 and -0.6). This shows that 1T-MoS_2 is a peculiar material, with a more complex affinity towards the ions than carbonaceous systems. Secondly, the charging mechanism is radically different in the positive electrode depending on whether or not the electronegativity of atoms is taken into account. In the conventional CPM model, we recover X-values around 0.3, indicating a usual ion exchange-dominated mechanism. On the contrary, using the CPM_χ model we obtain values of -0.75 and -1.0 at positive potentials which shows that the charging is then almost entirely due to the desorption of co-ions. This difference between the two models shows that reproducing

the experimental capacitance is not enough to validate MD simulations, since similar values can arise from very different mechanisms.

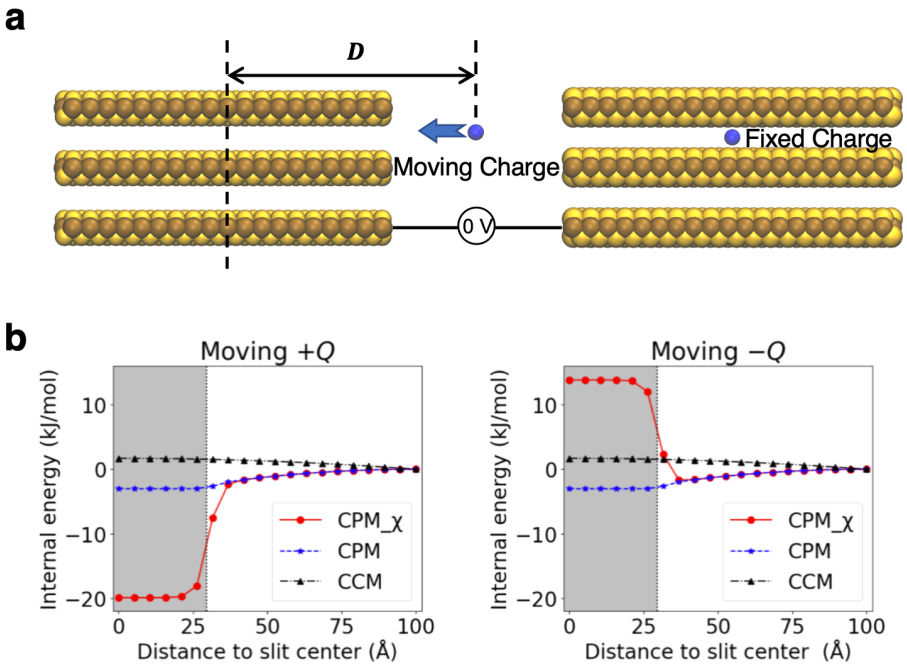

Fig. 5. Internal energies variations for adsorbing an external charge inside the electrode. a, Schematics of the slit test systems. **b**, Energetic profiles for moving a +0.1e charge (left) and a -0.1e charge (right) into the center of the left electrode in the slit system. The two charges are of the same magnitude (0.1 e) and opposite sign. The fixed charge is anchored in the center of the right electrode. The gray-shaped areas in panel b represent the regions of the electrode.

To understand deeper the origin of the peculiar charging mechanism, which is dominated by co-ion desorption unlike other materials, we study the energetics of single ion adsorption inside the 1T-MoS_2 nanosheets as illustrated in **Fig. 5a**. We simulate a system consisting in a pair of charges (+0.1 e and -0.1 e); one of them is anchored near or inside the right electrode, the other is initially placed in the vacuum region of the system. The electrodes and the two charges were frozen in the simulation to eliminate the kinetic component of the total energy, and the two charges have no other interactions with the electrodes except for the electrostatic interaction. The electrode potential of the two electrodes was set to 0 V using both CPM_χ and CPM. For comparison purposes, a contrast case of constant-charge-method (CCM)

simulation with zero charge on the electrode atoms and with no constant-potential constraint was also performed. The latter therefore allows us to unravel the ion-ion interaction due to the presence of two charges. We then dragged the charge progressively from the vacuum region toward or into the left electrode, and at each step computed the internal energy of system (**Fig. 5b**). In the conventional CPM simulation, it can be seen that there is a small stabilization of the charge upon entrance into the nanosheet: the internal energy decreases by a few kJ/mol, then it becomes stable as the charge is displaced into the nanosheets and moves to the center of the electrode (regardless of its sign). This means both positive and negative charges have an identical attractive interaction with the electrode. The small stabilization is consistent with the low values of partial charges on the MoS_2 electrode atoms in the CPM case, as was already evidenced on **Fig. 3**. In contrast, in the CPM_χ case, the slit electrode does not energetically favor the entrance of the negative charge as the internal energy increases by more than 10 kJ/mol when moving it from the vacuum region to the interior of the slit. On the contrary, the slit electrode displays a stronger attractive interaction with the positive charge compared to what we see in the CPM case, as it is stabilized by approximately 20 kJ/mol. This difference can be attributed to the large difference of electronegativity of the Mo and S atoms in the MoS_2 electrode. The resulting negative charge on the S atoms has a strong influence on the ability of cations and anions to enter into the nanosheets. We note however that the effect is not strong enough to render them truly ionophobic, since at 0 V the ions remain adsorbed at almost the same concentration as in the CPM case. This is due to the importance of ion-ion interactions, that remain stronger than the ion-electrode interactions as discussed in several other works.[41] The cations being attracted by the S atoms, they drag some anions with them inside the nanosheets despite the energy penalty associated to the adsorption of the latter.

Structure of the adsorbed liquid within the nanosheet

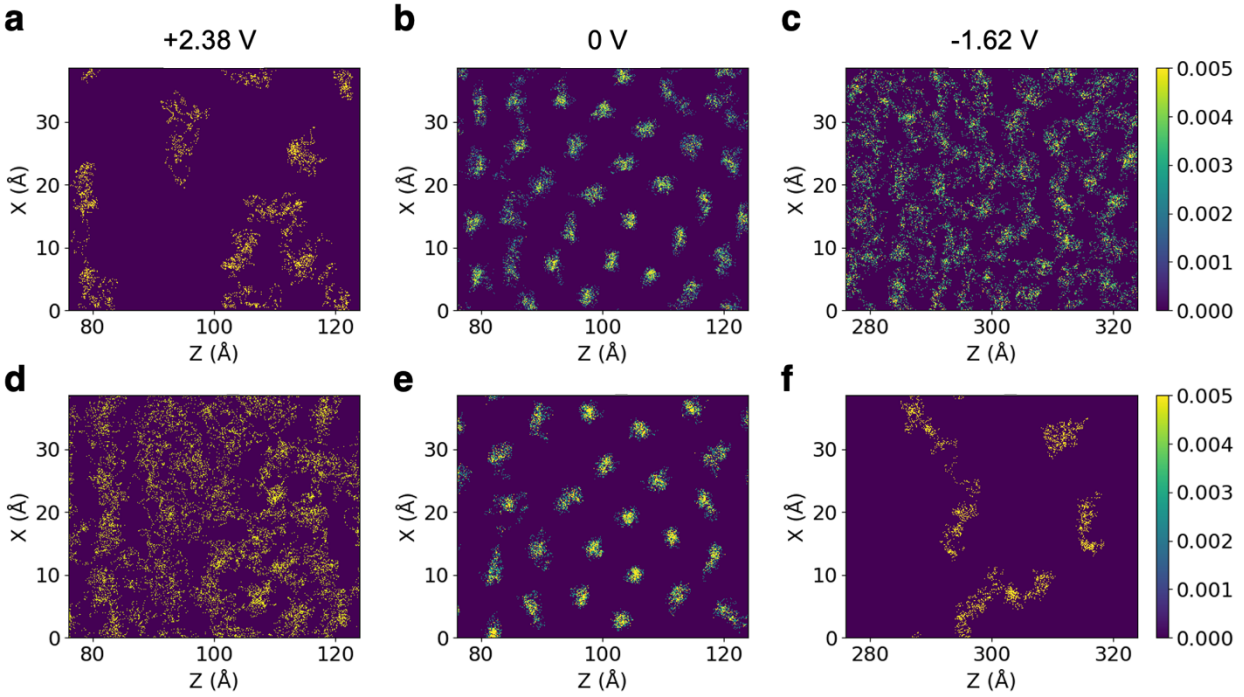

Fig. 6. In-slit ion density distribution inside 1T-MoS_2 nanosheets using the CPM_χ method. In-plane, 2D maps of cations $[EMIM]^+$ (**a,b,c**) and anion $[BF_4]^-$ (**d,e,f**) inside the 1T-MoS_2 nanosheets, at various electrode potentials (left: +2.38 V; middle: 0 V; right: -1.62 V). The analysis was performed on the central part of the electrodes (see its definition on **Fig. 1**).

We now focus on the structure of the adsorbed liquid in the case of the CPM_χ method. As electrolyte ions are confined between two 1T-MoS_2 layers with interlayer spacing of 0.8 nm, the charge distribution on electrode atoms may play a role in the structural properties of the intercalated electrolyte ions. But how significant can this effect be? **Fig. 6** shows the in-slit ion density distributions obtained with the CPM_χ under various applied electric potentials. Note that to minimize effects due to the finite size of the MoS_2 nanosheets in the simulations, only ions that are located in the central part of the slit-shape electrodes are sampled in our analysis (see **Fig. 1** for details). The densities are averaged over a time range of 100 ps; taking a larger range would lead to blurred profiles in which it would not be possible to distinguish specific structural arrangements.

If we first focus on the null potential case, the adsorbed ionic liquid displays a rather ordered structure, reminiscent of the one which was observed in the case of graphene-based slit pores.[43–45] This is due to the dual constraint imposed by the nanoporosity and by the Coulomb ordering: On the one hand, all the ions are forced to lie in the same plane while on the other hand every cation will tend to be surrounded by anions and vice-versa. Once a potential is applied, due to the charging mechanism dominated by co-ion desorption, the density of cations in the positive electrode (**Fig. 6a**) and of anions in the negative electrode (**Fig. 6f**) become much sparser, with some regions with area larger than 1 nm^2 left unoccupied. As expected from the previous analysis, the effect is much more pronounced in the negative electrode due to the low affinity of anions for the S-based surface. Now focusing on the structure adopted by counter-ions (**Fig. 6c, 6d**), we observe that it is much more disordered than the one obtained at 0 V (**Fig. 6b**, **6e**). This occurs despite the fact that their number does not increase significantly, and can be attributed to the presence of a larger accessible volume due to the leave of co-ions.

Assessing the impact of the nanoconfinement

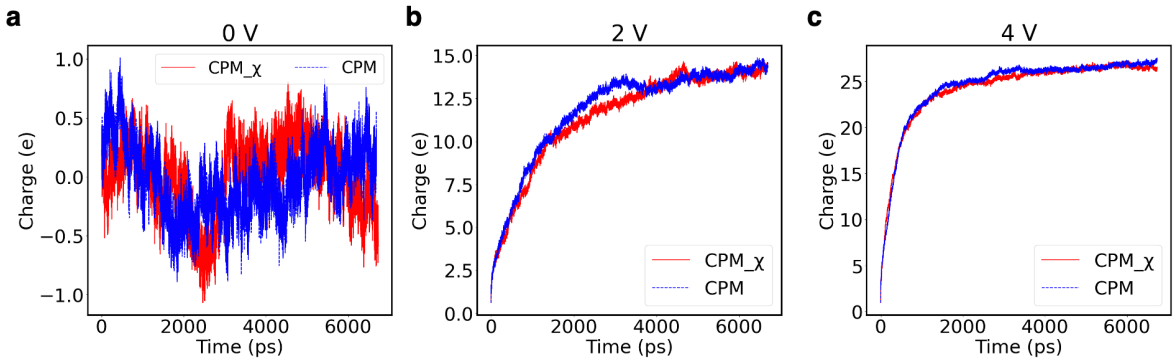

Fig. 7. Charging dynamics in slab simulations. Time evolutions of the electrode total charge, after a voltage of 0 V (**a**), 2 V (**b**) and 4 V (**c**) were applied between two electrodes.

Now that we have established the effect of the atoms electronegativity on the charging mechanism of slit-shaped 1T-MoS_2, it is of interest to determine the impact of nanoconfinement on the results. Indeed, as shown on **Fig. 5b**, the different stabilization energies for cations and anions occur upon their entrance into the nanosheets. We have therefore performed further simulations of electrified slab-like MoS_2 in contact

with the same ionic liquid electrolyte (simulation setup, see **Fig. 1b**). Albeit this system is not very important technologically, it provides an interesting comparison with the 1T-MoS_2 case. Indeed, for the slab geometry, both the CPM and CPM_χ methods yield almost similar results, not only for the capacitance but also for the adsorbed ionic liquid structure at various potentials. The capacitive behavior can be analyzed from **Fig. 7**, that respectively compare the CPM_χ with the original CPM with respect to the time evolutions of the total electrode charges at equilibrium under 0 V applied potential and upon application of finite voltages of 2 V and 4 V. The results obtained by the two methods show minor difference when compared to each other. These findings indicate that for systems with planar MoS_2 electrodes, the chemical potential difference between the electrode elements does not manifest and barely affects the charging dynamic behaviors of the systems.

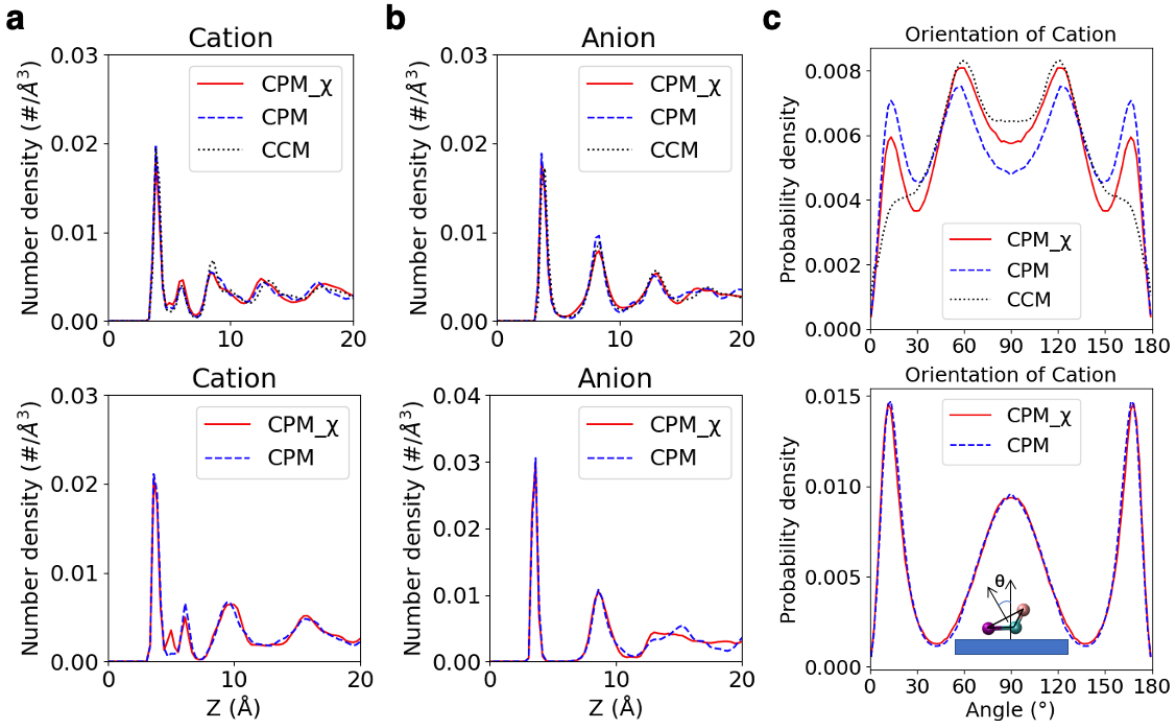

Fig. 8. Ion density and orientation distribution in slab simulations. a, **b**, Cation $[EMIM]^+$ (**a**) and anion $[BF_4]^-$ (**b**) number density profiles near the slab-shape MoS_2 surface. **c**, Angular distributions of the interfacial cations that are within 3.9 Å from the electrode surface. The upper panels and the lower panels are results when electric potential between two electrodes is 0 V and 2 V, respectively.

However, such a result was expected since we did not observe quantitative differences in the total charges of 1T-MoS_2 either. We further compare the structures of the electrolyte ions near the MoS_2 surface on **Fig. 8**. Under zero polarization, it can be seen that the 1D ion distributions obtained by the two approaches are almost similar (**Fig. 8a, b**, upper panels), both for cations and anions. When focusing on the 'interfacial cations' that are within the 1st adsorption layer and analyzing their orientations (**Fig. 8c**, upper panels), still the two methods give the same characteristic angles despite minor discrepancies in the distributions. Such comparisons are also made under a 2 V applied electrode voltages (**Fig. 8**, lower panels), and the two methods give quite even more similar structural results.

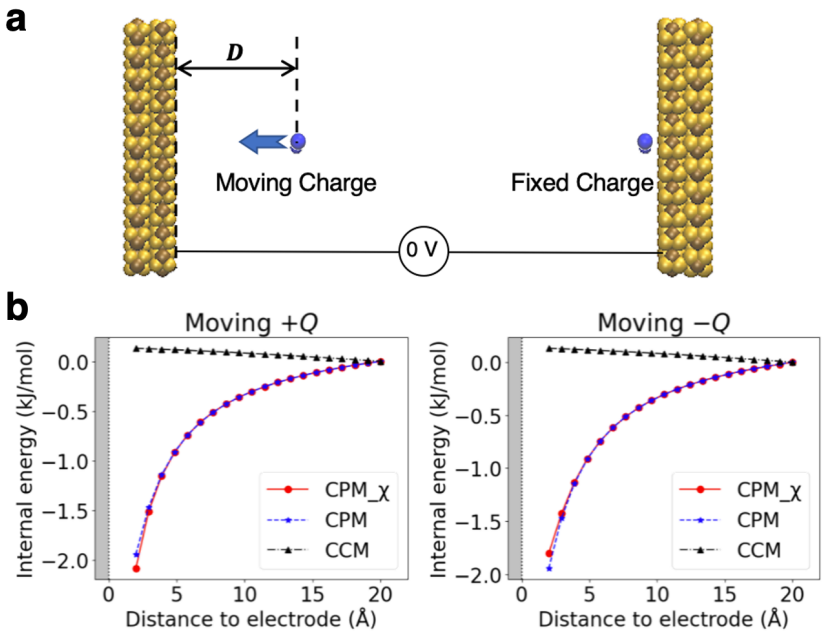

Fig. 9. Internal energies for moving an external charge towards the slab electrode. a, Schematics of the slab test systems. **b**, Energy profiles for moving a +0.1e charge (left) and a -0.1e charge (right) towards the left electrode surface in the slab system. The two charges are of the same magnitude (0.1 e) and opposite sign. The fixed charge is anchored 2 Å away from the right electrode.

In order to understand why in the case of this slab system there is no difference on the structure of the adsorbed fluid, we have therefore performed a similar energy analysis as for the nanosheets, by approaching a charge progressively towards the electrode. As shown on **Fig. 9b**, despite deviations when the charge is

extremely close to the electrode surface (less than 4 Å), the internal energy curves do not see obvious difference in the CPM_χ and CPM cases. Also, both methods give almost identical internal energy profiles regardless of the sign of the moving charge. The results reveal that the CPM_χ method does not make the electrodes more energetically favorable or unfavorable to the external charges in the slab-configuration simulations. Therefore, we do not see obvious distinctions in the structural and charging dynamic properties obtained by the CPM_χ and the original CPM simulations. This effect may not be generic since we consider species with relatively large ionic dimensions (~5 Å).[46] Due to this structural feature, the ions of the ionic liquid cannot approach very close to the electrode; in our cases, the first adsorbed layer of cations and anions are, respectively, 3.9 Å and 3.7 Å, away from the electrode surface. For this reason, the structural results obtained in the CPM simulation do not deviate much from those obtained in the simulation with zero charge on the electrode atoms and without constant-potential constraint (**Fig. 8**, upper panels), evidencing that the image charge effects are not strong if the ions are that far away from the electrode. Therefore, it is not surprising that the IL ions may not be able to perceive the potential difference at different electrode atoms in systems with slab configuration.

Conclusion

We have investigated the capacitance and charging mechanism of supercapacitors consisting of metallic 1T-MoS_2 nanosheets and ionic liquid electrolyte via MD simulations at fixed electrochemical potentials. In agreement with experiments, the simulations yield a high volumetric capacitance (113 F/cm^3) for 1T-MoS_2, confirming its great potential as an electrode material in supercapacitors. Moreover, our simulations reveal that it has a peculiar charging mechanism: the desorption of co-ion is much more pronounced than the adsorption of counterions during the charging process; in particular, it dominates over counterion adsorption under positive polarization. This mechanism differs to the one observed when neglecting the electronegativity of the Mo and S atoms, for which the usual ion exchange mechanism is obtained at positive electrode polarizations. This difference originates from the large gap in the electronegativity of the two

elements in MoS_2, which leads to a significant negative charge on the S atoms thus imposing an asymmetrical impact on the entering of cations and anions.

Interestingly, the electronegativity effects are found to be negligible in the simulations of electrified slab-like MoS_2. The microstructures of electrolyte ions near the electrode, including ion distribution and ion orientations, are similar to the case of conventional constant potential conditions, suggesting that nanoconfinement is necessary for observing the consequences of the different affinities of the ions towards the surface. The findings reported are not only helpful for the fundamental understanding of charge storage of 1T-MoS_2 in ionic liquids, but the approach can easily be extended in future MD simulation studies involving complex electrode materials, such as MXenes or other 2D layered materials.

Methods

Constant-potential method with tunable Gaussian width and electronegativity

In Siepmann and Sprik's original CPM,[47] the charges on the electrode atoms are described by the Gaussian charge distributions (Eq. 1).

$$\rho_i(r) = q_i(2\pi\sigma^2)^{-\frac{3}{2}} e^{-\frac{|\mathbf{r}-\mathbf{r_i}|^2}{2\sigma^2}} \quad (1)$$

where σ is the width of the distribution and $\mathbf{r_i}$ is the position of atom i. In the original CPM, the application of an electrical potential Φ_i on each atom has been achieved by the following constraints (Eq. 2)

$$V = \Phi_i = \frac{\partial U}{\partial q_i} \quad (2)$$

where U is the total Coulombic energy of the system.

In our simulations, we first assign different values of Gaussian widths σ to the two elements in MoS_2 electrode (see Table. 1). These values are taken from the set of covalent atomic radii developed by Santiago and their co-workers.[48] Also, the original electrical potential constraints are modified to Eq. 3, in which the derivative of U with respect to the charge of atom i is set to be equal to the sum of an applied electrical potential and the electronegativity of this element, which is also often named electrochemical potential μ.

$$\mu_i = \Phi_i + \chi_i = \frac{\partial U}{\partial q_i} \quad (3)$$

The electronegativities for different elements ($\boldsymbol{\chi}$, vector of the electronegativity values for the electrode atoms) are obtained by solving the following matrix equation (Eq. 4),

$$\boldsymbol{\chi} = \mathbf{AQ} \quad (4)$$

where **A** is a pre-calculated Matrix which depends only on the geometry of the electrodes (also used in the original CPM method),[49] and **Q** is the vector of electrode atom partial charges (q_{Mo} and q_s, see Table 1) which comes from the previous density functional theory calculation on MoS_2.[37] The computed electronegativity values are also summarized in the Table. 1.

Table 1. Partial charge, Gaussian width of atom Mo and S.

Element	Partial charge (e)[a]	Gaussian width (Å)[b]	Electronegativity (V)
Mo	0.60	1.54	3.03
S	0.30	1.05	1.51

[a] values taken from ref [37]

[b] values taken from ref [48]

Simulation setup and details

All simulations were performed using the molecular dynamics package MetalWalls.[50] As shown in Fig. 1, two different types of systems were simulated. In one case, the system embeds two planar MoS_2 electrodes with the electrolyte confined between them; in the other case, the system is composed of two slit-shape MoS_2 electrodes emerged in the electrolyte. In the former system, the electrolyte ions are adsorbed on the surface of MoS_2 whereas in the latter system, the ions are intercalated into the spacing of MoS_2 layers. The Lennard-Jones parameters for the electrode atoms were taken from the Aluru's work;[37] the coarse-grained model, which provides accurate thermodynamic and dynamic properties, was adopted for [Emim][BF_4].[51] For both configurations, the simulation cells were chosen large enough to reproduce the bulk state in the central region of the electrolyte reservoir connected with two electrodes, and periodic boundary conditions were applied in all directions. Specific system parameters are given in **Fig. 1**.

The simulations were performed in the NVT ensemble with a time step of 2 fs; a Nosé–Hoover thermostat chain was used with a time constant of 1 ps to maintain a temperature of 298 K. To guarantee accuracy, the electrode charges were updated on-the-fly every simulation step. A cutoff length of 1.2 nm was used in the direct summation of the non-electrostatic interactions and electrostatic interactions in real space. All the MD simulations went through a 10-ns relaxation to reach equilibrium under null electrode potential. To explore the charging dynamics, three independent runs were performed to smooth the charging process data. To obtain microstructures, simulations were first performed for 20 ns to ensure reaching equilibrium under the applied potential ranging from 0 to 4 V, and then 20-ns production runs in the equilibrium state were carried out for analysis.

Acknowledgments

This project has received funding from the European Research Council (ERC) under the European Union's Horizon 2020 research and innovation programme (grant agreements No. 771294 and 863473). This work was supported by the French National Research Agency (Labex STORE-EX, Grant ANR-10-LABX-0076). This work was granted access to the HPC resources of CINES under Allocation A0120910463 made by GENCI.

Data availability

The code used for the simulations and the data that support the findings of this study are openly available in the repository https://gitlab.com/ampere2.

References

(1) Choi, W.; Choudhary, N.; Han, G. H.; Park, J.; Akinwande, D.; Lee, Y. H. Recent Development of Two-Dimensional Transition Metal Dichalcogenides and Their Applications. *Mater. Today* **2017**, *20* (3), 116–130. https://doi.org/https://doi.org/10.1016/j.mattod.2016.10.002.

(2) Wang, Q. H.; Kalantar-Zadeh, K.; Kis, A.; Coleman, J. N.; Strano, M. S. Electronics and Optoelectronics of Two-Dimensional Transition Metal Dichalcogenides. *Nat. Nanotechnol.* **2012**, *7* (11), 699–712. https://doi.org/10.1038/nnano.2012.193.

(3) Ganatra, R.; Zhang, Q. Few-Layer MoS_2: A Promising Layered Semiconductor. *ACS Nano* **2014**, *8* (5), 4074–4099. https://doi.org/10.1021/nn405938z.

(4) Wang, Z.; Mi, B. Environmental Applications of 2D Molybdenum Disulfide (MoS_2) Nanosheets. *Environ. Sci. Technol.* **2017**, *51* (15), 8229–8244. https://doi.org/10.1021/acs.est.7b01466.

(5) Gupta, D.; Chauhan, V.; Kumar, R. A Comprehensive Review on Synthesis and Applications of Molybdenum Disulfide (MoS_2) Material: Past and Recent Developments. *Inorg. Chem. Commun.* **2020**, *121*, 108200. https://doi.org/https://doi.org/10.1016/j.inoche.2020.108200.

(6) Yang, X.; Li, Q.; Hu, G.; Wang, Z.; Yang, Z.; Liu, X.; Dong, M.; Pan, C. Controlled Synthesis of High-Quality Crystals of Monolayer MoS_2 for Nanoelectronic Device Application. *Sci. China Mater.* **2016**, *59* (3), 182–190. https://doi.org/10.1007/s40843-016-0130-1.

(7) Bilgin, I.; Liu, F.; Vargas, A.; Winchester, A.; Man, M. K. L.; Upmanyu, M.; Dani, K. M.; Gupta, G.; Talapatra, S.; Mohite, A. D.; Kar, S. Chemical Vapor Deposition Synthesized Atomically Thin Molybdenum Disulfide with Optoelectronic-Grade Crystalline Quality. *ACS Nano* **2015**, *9* (9), 8822–8832. https://doi.org/10.1021/acsnano.5b02019.

(8) Goodfellow, K. M.; Beams, R.; Chakraborty, C.; Novotny, L.; Vamivakas, A. N. Integrated Nanophotonics Based on Nanowire Plasmons and Atomically Thin Material. *Optica* **2014**, *1* (3), 149–152. https://doi.org/10.1364/OPTICA.1.000149.

(9) Zhang, H.; Lu, S. B.; Zheng, J.; Du, J.; Wen, S. C.; Tang, D. Y.; Loh, K. P. Molybdenum Disulfide (MoS_2) as a Broadband Saturable Absorber for Ultra-Fast Photonics. *Opt. Express* **2014**, *22* (6), 7249–7260. https://doi.org/10.1364/OE.22.007249.

(10) Lee, K.; Gatensby, R.; McEvoy, N.; Hallam, T.; Duesberg, G. S. High-Performance Sensors Based on Molybdenum Disulfide Thin Films. *Adv. Mater.* **2013**, *25* (46), 6699–6702. https://doi.org/https://doi.org/10.1002/adma.201303230.

(11) Agrawal, A. V; Kumar, N.; Kumar, M. Strategy and Future Prospects to Develop Room-Temperature-Recoverable NO_2 Gas Sensor Based on Two-Dimensional Molybdenum Disulfide. *Nano-Micro Lett.* **2021**, *13* (1), 38. https://doi.org/10.1007/s40820-020-00558-3.

(12) Yin, Y.; Han, J.; Zhang, Y.; Zhang, X.; Xu, P.; Yuan, Q.; Samad, L.; Wang, X.; Wang, Y.; Zhang,

Z.; Zhang, P.; Cao, X.; Song, B.; Jin, S. Contributions of Phase, Sulfur Vacancies, and Edges to the Hydrogen Evolution Reaction Catalytic Activity of Porous Molybdenum Disulfide Nanosheets. *J. Am. Chem. Soc.* **2016**, *138* (25), 7965–7972. https://doi.org/10.1021/jacs.6b03714.

(13) Yang, T.; Song, T. T.; Zhou, J.; Wang, S.; Chi, D.; Shen, L.; Yang, M.; Feng, Y. P. High-Throughput Screening of Transition Metal Single Atom Catalysts Anchored on Molybdenum Disulfide for Nitrogen Fixation. *Nano Energy* **2020**, *68*, 104304. https://doi.org/10.1016/j.nanoen.2019.104304.

(14) Hirunpinyopas, W.; Prestat, E.; Worrall, S. D.; Haigh, S. J.; Dryfe, R. A. W.; Bissett, M. A. Desalination and Nanofiltration through Functionalized Laminar MoS_2 Membranes. *ACS Nano* **2017**, *11* (11), 11082–11090. https://doi.org/10.1021/acsnano.7b05124.

(15) Li, W.; Yang, Y.; Weber, J. K.; Zhang, G.; Zhou, R. Tunable, Strain-Controlled Nanoporous MoS_2 Filter for Water Desalination. *ACS Nano* **2016**, *10* (2), 1829–1835. https://doi.org/10.1021/acsnano.5b05250.

(16) Kappera, R.; Voiry, D.; Yalcin, S. E.; Jen, W.; Acerce, M.; Torrel, S.; Branch, B.; Lei, S.; Chen, W.; Najmaei, S.; Lou, J.; Ajayan, P. M.; Gupta, G.; Mohite, A. D.; Chhowalla, M. Metallic 1T Phase Source/Drain Electrodes for Field Effect Transistors from Chemical Vapor Deposited MoS_2. *APL Mater.* **2014**, *2* (9). https://doi.org/10.1063/1.4896077.

(17) Acerce, M.; Voiry, D.; Chhowalla, M. Metallic 1T Phase MoS_2 Nanosheets as Supercapacitor Electrode Materials. *Nat. Nanotechnol.* **2015**, *10* (4), 313–318. https://doi.org/10.1038/nnano.2015.40.

(18) Wang, T.; Chen, S.; Pang, H.; Xue, H.; Yu, Y. MoS_2-Based Nanocomposites for Electrochemical Energy Storage. *Adv. Sci.* **2017**, *4* (2). https://doi.org/10.1002/advs.201600289.

(19) Wang, P.; Sun, S.; Jiang, Y.; Cai, Q.; Zhang, Y. H.; Zhou, L.; Fang, S.; Liu, J.; Yu, Y. Hierarchical Microtubes Constructed by MoS_2 Nanosheets with Enhanced Sodium Storage Performance. *ACS Nano* **2020**, *14* (11), 15577–15586. https://doi.org/10.1021/acsnano.0c06250.

(20) Jiao, Y.; Hafez, A. M.; Cao, D.; Mukhopadhyay, A.; Ma, Y.; Zhu, H. Metallic MoS_2 for High Performance Energy Storage and Energy Conversion. *Small* **2018**, *14* (36), 1800640. https://doi.org/https://doi.org/10.1002/smll.201800640.

(21) Simon, P.; Gogotsi, Y. Materials for Electrochemical Capacitors. *Nat. Mater.* **2008**, *7* (11), 845–854. https://doi.org/10.1038/nmat2297.

(22) Bhimanapati, G. R.; Lin, Z.; Meunier, V.; Jung, Y.; Cha, J.; Das, S.; Xiao, D.; Son, Y.; Strano, M. S.; Cooper, V. R.; Liang, L.; Louie, S. G.; Ringe, E.; Zhou, W.; Kim, S. S.; Naik, R. R.; Sumpter, B. G.; Terrones, H.; Xia, F.; Wang, Y.; Zhu, J.; Akinwande, D.; Alem, N.; Schuller, J. A.; Schaak, R. E.; Terrones, M.; Robinson, J. A. Recent Advances in Two-Dimensional Materials beyond

Graphene. *ACS Nano* **2015**, *9* (12), 11509–11539. https://doi.org/10.1021/acsnano.5b05556.

(23) Simon, P.; Gogotsi, Y. Perspectives for Electrochemical Capacitors and Related Devices. *Nat. Mater.* **2020**, *19* (11), 1151–1163. https://doi.org/10.1038/s41563-020-0747-z.

(24) Jeanmairet, G.; Rotenberg, B.; Salanne, M. Microscopic Simulations of Electrochemical Double-Layer Capacitors. *Chem. Rev.* **2022**, *122* (12), 10860–10898. https://doi.org/10.1021/acs.chemrev.1c00925.

(25) Vatamanu, J.; Vatamanu, M.; Bedrov, D. Non-Faradaic Energy Storage by Room Temperature Ionic Liquids in Nanoporous Electrodes. *ACS Nano* **2015**, *9* (6), 5999–6017. https://doi.org/10.1021/acsnano.5b00945.

(26) Vatamanu, J.; Bedrov, D. Capacitive Energy Storage: Current and Future Challenges. *J. Phys. Chem. Lett.* **2015**, *6* (18), 3594–3609. https://doi.org/10.1021/acs.jpclett.5b01199.

(27) Scalfi, L.; Salanne, M.; Rotenberg, B. Molecular Simulation of Electrode-Solution Interfaces. *Annu. Rev. Phys. Chem.* **2020**, *72*, 189–212. https://doi.org/10.1146/annurev-physchem-090519-024042.

(28) Merlet, C.; Péan, C.; Rotenberg, B.; Madden, P. A.; Simon, P.; Salanne, M. Simulating Supercapacitors: Can We Model Electrodes as Constant Charge Surfaces? *J. Phys. Chem. Lett.* **2013**, *4* (2), 264–268. https://doi.org/10.1021/jz3019226.

(29) Bedrov, D.; Piquemal, J.-P.; Borodin, O.; MacKerell, A. D.; Roux, B.; Schröder, C. Molecular Dynamics Simulations of Ionic Liquids and Electrolytes Using Polarizable Force Fields. *Chem. Rev.* **2019**, *119* (13), 7940–7995. https://doi.org/10.1021/acs.chemrev.8b00763.

(30) Liu, Y. M.; Merlet, C.; Smit, B. Carbons with Regular Pore Geometry Yield Fundamental Insights into Supercapacitor Charge Storage. *ACS Cent. Sci.* **2019**, *5* (11), 1813–1823. https://doi.org/10.1021/acscentsci.9b00800.

(31) Onofrio, N.; Strachan, A. Voltage Equilibration for Reactive Atomistic Simulations of Electrochemical Processes. *J. Chem. Phys.* **2015**, *143* (5), 54109. https://doi.org/10.1063/1.4927562.

(32) Pean, C.; Daffos, B.; Rotenberg, B.; Levitz, P.; Haefele, M.; Taberna, P. L.; Simon, P.; Salanne, M. Confinement, Desolvation, and Electrosorption Effects on the Diffusion of Ions in Nanoporous Carbon Electrodes. *J. Am. Chem. Soc.* **2015**, *137* (39), 12627–12632. https://doi.org/10.1021/jacs.5b07416.

(33) Méndez-Morales, T.; Ganfoud, N.; Li, Z.; Haefele, M.; Rotenberg, B.; Salanne, M. Performance of Microporous Carbon Electrodes for Supercapacitors: Comparing Graphene with Disordered Materials. *Energy Storage Mater.* **2019**, *17*, 88–92. https://doi.org/10.1016/j.ensm.2018.11.022.

(34) Bi, S.; Banda, H.; Chen, M.; Niu, L.; Chen, M.; Wu, T.; Wang, J.; Wang, R.; Feng, J.; Chen, T.;

Dincă, M.; Kornyshev, A. A.; Feng, G. Molecular Understanding of Charge Storage and Charging Dynamics in Supercapacitors with MOF Electrodes and Ionic Liquid Electrolytes. *Nat. Mater.* **2020**, *19* (5), 552–558. https://doi.org/10.1038/s41563-019-0598-7.

(35) Barik, R.; Ingole, P. P. Challenges and Prospects of Metal Sulfide Materials for Supercapacitors. *Curr. Opin. Electrochem.* **2020**, *21*, 327–334. https://doi.org/10.1016/j.coelec.2020.03.022.

(36) Gao, Y.; Zhao, L. Review on Recent Advances in Nanostructured Transition-Metal-Sulfide-Based Electrode Materials for Cathode Materials of Asymmetric Supercapacitors. *Chem. Eng. J.* **2022**, *430* (P2), 132745. https://doi.org/10.1016/j.cej.2021.132745.

(37) Heiranian, M.; Wu, Y.; Aluru, N. R. Molybdenum Disulfide and Water Interaction Parameters. *J. Chem. Phys.* **2017**, *147* (10). https://doi.org/10.1063/1.5001264.

(38) Tocci, G.; Bilichenko, M.; Joly, L.; Iannuzzi, M. Ab Initio Nanofluidics: Disentangling the Role of the Energy Landscape and of Density Correlations on Liquid/Solid Friction. *Nanoscale* **2020**, *12* (20), 10994–11000. https://doi.org/10.1039/D0NR02511A.

(39) Forse, A. C.; Merlet, C.; Griffin, J. M.; Grey, C. P. New Perspectives on the Charging Mechanisms of Supercapacitors. *J. Am. Chem. Soc.* **2016**, *138* (18), 5731–5744. https://doi.org/10.1021/jacs.6b02115.

(40) Forse, A. C.; Griffin, J. M.; Merlet, C.; Carretero-Gonzalez, J.; Raji, A. R. O.; Trease, N. M.; Grey, C. P. Direct Observation of Ion Dynamics in Supercapacitor Electrodes Using in Situ Diffusion NMR Spectroscopy. *Nat. Energy* **2017**, *2* (3), 1–7. https://doi.org/10.1038/nenergy.2016.216.

(41) Burt, R.; Breitsprecher, K.; Daffos, B.; Taberna, P. L.; Simon, P.; Birkett, G.; Zhao, X. S.; Holm, C.; Salanne, M. Capacitance of Nanoporous Carbon-Based Supercapacitors Is a Trade-Off between the Concentration and the Separability of the Ions. *J. Phys. Chem. Lett.* **2016**, *7* (19), 4015–4021. https://doi.org/10.1021/acs.jpclett.6b01787.

(42) Levi, M. D.; Levy, N.; Sigalov, S.; Salitra, G.; Aurbach, D.; Maier, J. Electrochemical Quartz Crystal Microbalance (EQCM) Studies of Ions and Solvents Insertion into Highly Porous Activated Carbons. *J. Am. Chem. Soc.* **2010**, *132* (38), 13220–13222. https://doi.org/10.1021/ja104391g.

(43) Pereira, G. F. L.; Pereira, R. G.; Salanne, M.; Siqueira, L. J. A. Molecular Dynamics Simulations of Ether-Modified Phosphonium Ionic Liquid Confined in between Planar and Porous Graphene Electrode Models. *J. Phys. Chem. C* **2019**, *123* (17), 10816–10825. https://doi.org/10.1021/acs.jpcc.9b01821.

(44) Kondrat, S.; Wu, P.; Qiao, R.; Kornyshev, A. A. Accelerating Charging Dynamics in Subnanometre Pores. *Nat. Mater.* **2014**, *13* (4), 387–393. https://doi.org/10.1038/nmat3916.

(45) Vatamanu, J.; Borodin, O.; Olguin, M.; Yushin, G.; Bedrov, D. Charge Storage at the Nanoscale: Understanding the Trends from the Molecular Scale Perspective. *J. Mater. Chem. A* **2017**, *5* (40), 21049–21076. https://doi.org/10.1039/C7TA05153K.

(46) Zhang, S.; Sun, N.; He, X.; Lu, X.; Zhang, X. Physical Properties of Ionic Liquids: Database and Evaluation. *J. Phys. Chem. Ref. Data* **2006**, *35* (4), 1475–1517. https://doi.org/10.1063/1.2204959.

(47) Siepmann, J. I.; Sprik, M. Influence of Surface Topology and Electrostatic Potential on Water/Electrode Systems. *J. Chem. Phys.* **1995**, *102* (1), 511–524. https://doi.org/10.1063/1.469429.

(48) Cordero, B.; Gómez, V.; Platero-Prats, A. E.; Revés, M.; Echeverría, J.; Cremades, E.; Barragán, F.; Alvarez, S. Covalent Radii Revisited. *Dalt. Trans.* **2008**, 2832–2838. https://doi.org/10.1039/b801115j.

(49) Scalfi, L.; Limmer, D. T.; Coretti, A.; Bonella, S.; Madden, P. A.; Salanne, M.; Rotenberg, B. Charge Fluctuations from Molecular Simulations in the Constant-Potential Ensemble. *Phys. Chem. Chem. Phys.* **2020**, *22* (19), 10480–10489. https://doi.org/10.1039/C9CP06285H.

(50) Marin-Laflèche, A.; Haefele, M.; Scalfi, L.; Coretti, A.; Dufils, T.; Jeanmairet, G.; Reed, S.; Serva, A.; Berthin, R.; Bacon, C.; Bonella, S.; Rotenberg, B.; Madden, P.; Salanne, M. MetalWalls: A Classical Molecular Dynamics Software Dedicated to the Simulation of Electrochemical Systems. *J. Open Source Softw.* **2020**, *5* (53), 2373. https://doi.org/10.21105/joss.02373.

(51) Merlet, C.; Salanne, M.; Rotenberg, B. New Coarse-Grained Models of Imidazolium Ionic Liquids for Bulk and Interfacial Molecular Simulations. *J. Phys. Chem. C* **2012**, *116* (14), 7687–7693. https://doi.org/10.1021/jp3008877.